

# Coherent two-photon emission from hydrogen molecules excited by counter-propagating laser pulses

Takahiro Hiraki<sup>1</sup>, Hideaki Hara<sup>1</sup>, Yuki Miyamoto<sup>1</sup>,  
Kei Imamura<sup>1</sup>, Takahiko Masuda<sup>1</sup>, Noboru Sasao<sup>1</sup>,  
Satoshi Uetake<sup>1,2</sup>, Akihiro Yoshimi<sup>1</sup>, Koji Yoshimura<sup>1</sup>, and  
Motohiko Yoshimura<sup>1</sup>

<sup>1</sup> Research Institute for Interdisciplinary Science, Okayama University, Okayama 700-8530, Japan

<sup>2</sup> PRESTO, Japan Science and Technology, Okayama 700-8530, Japan

E-mail: [thiraki@okayama-u.ac.jp](mailto:thiraki@okayama-u.ac.jp)

June 2018

**Abstract.** We observed two-photon emission signals from the first vibrationally excited state of parahydrogen gas excited coherently by counter-propagating laser pulses. A single narrow-linewidth laser source was used to excite the parahydrogen molecules and induce the two-photon emission process. We measured how the signal energy depended on the detuning, target gas pressure, and input pulse energies. These results are qualitatively consistent with those obtained by numerical simulations based on the Maxwell–Bloch equations with one spatial dimension and one temporal dimension. This study of two-photon emission with counter-propagating injection is an important step toward neutrino mass spectroscopy.

*Keywords:* coherence, parahydrogen, two-photon emission, counter-propagating laser injection, Maxwell–Bloch equations

## 1. Introduction

The emission processes of atoms or molecules can be modified if they involve coherent phenomena. A well-known example is superradiance, which was first predicted by Dicke [1] and has been observed in various systems [2–9]. In superradiant emission, an ensemble of atoms or molecules behaves cooperatively. Consequently, the emission rate of the ensemble is enhanced considerably compared with the usual cases in which each atom or molecule behaves independently [10]. By taking advantage of this

enhancement property of superradiance, very weak processes of atomic transitions can be observed [11].

One of the present authors has proposed another coherent amplification scheme [12]. The principle of this scheme is reviewed in [13] and is described briefly here. Let us consider a system in which atoms or molecules are excited by lasers to a metastable excited state and then de-excite by emitting particles. In the excitation process, coherence among laser photons is imprinted into the ensemble. We denote by  $\mathbf{k}_{\text{in}}$  ( $\mathbf{k}_{\text{out}}$ ) the sum of the wavevectors of the excitation (de-excitation) particles. The emission rate  $R$  of this process is proportional to

$$\left| \int d\mathbf{r} \sum_{a=1}^N \exp(i(\mathbf{k}_{\text{in}} - \mathbf{k}_{\text{out}}) \cdot (\mathbf{r} - \mathbf{r}_a)) \mathcal{M}(\mathbf{r}_a) \right|^2, \quad (1)$$

where  $a$  denotes an atom or molecule,  $\mathbf{r}_a$  denotes its spatial position, and  $\mathcal{M}$  represents the transition amplitude of the atom at position  $\mathbf{r}_a$ . If each particle behaves independently, the emission rate is proportional to the total number  $N$  of atoms or molecules involved. However, if  $\mathbf{k}_{\text{in}} = \mathbf{k}_{\text{out}}$  and the decoherence time is sufficiently long, the emission rate becomes

$$R \propto \left| \sum_{a=1}^N \mathcal{M}(\mathbf{r}_a) \right|^2 \propto N^2 \quad (2)$$

and thus huge rate amplification can be achieved. Here, rate amplification is realized only if momentum  $\mathbf{k}_{\text{in}} = \mathbf{k}_{\text{out}}$  or there is conservation among the excitation and de-excitation particles.

This method of amplifying the emission rate could be used to resolve fundamental questions in a different context, namely, neutrino physics [13, 14]. In recent neutrino physics, the squared-mass differences and the mixing angles of neutrinos have been measured in various neutrino oscillation experiments [15–20]. However, the absolute mass scale, mass ordering, CP phases, and mass type (Dirac or Majorana) of neutrinos are yet to be explored experimentally [21–24]. Uncovering these properties is important for both particle physics beyond the standard model and cosmology [25]. We use atomic or molecular de-excitation processes that emit a single photon and a neutrino pair, which we call radiative emission of a neutrino pair (RENP). In RENP, the photon energy spectrum contains abundant information about the aforementioned neutrino properties [26, 27]. However, a serious issue when we use RENP processes in experiments is the fact that they have extremely small rates [14, 26, 28]. Therefore, using the proposed amplification method to amplify these rates would be key to observing RENP processes.

We have been studying the proposed coherent amplification mechanism with the aim of observing RENP processes. For this purpose, we have been measuring properties of the two-photon emission (TPE) process. It is easier to observe TPE processes than it is to observe RENP processes, mainly because the emission rates of the former are much higher.

In previous experiments, we observed the TPE signal from vibrational states of parahydrogen ( $\text{p-H}_2$ ) molecules [29–31], which have relatively long decoherence times

(of the order of a nanosecond). In those experiments, we injected two lasers of different colors coaxially in the same direction for the Raman excitation of p-H<sub>2</sub>. By contrast, in the present study we excite p-H<sub>2</sub> by monochromatic counter-propagating lasers. The present excitation scheme satisfies another requirement for amplifying RENP processes, as described below.

We focus on the invariant mass of the excitation and de-excitation particles in RENP processes. To amplify the emission rate, the invariant mass should be conserved. This is because, in addition to momentum conservation, energy conservation among the excitation and de-excitation particles should also hold. RENP processes occur only when the invariant mass exceeds the sum of the masses of the emitted neutrinos.

For the excitation, the squared invariant mass of the two free photons is given by

$$s = 2c^2|\mathbf{p}_1|^2|\mathbf{p}_2|^2(1 - \cos\theta), \quad (3)$$

where  $|\mathbf{p}_1|$  and  $|\mathbf{p}_2|$  indicate the momentum of each photon and  $\theta$  indicates the crossing angle between the photons. With one-sided laser injection ( $\theta = 0$ ),  $s$  is equal to zero and the RENP amplification conditions cannot be satisfied. By contrast, with counter-propagating laser excitation ( $\theta = \pi$ ) it is possible to satisfy the RENP amplification conditions. Another merit of the counter-propagating excitation scheme is related to soliton formulation, which is described in [32, 33]. For these reasons, observing and understanding TPE with counter-propagating injection would be an important step toward observing RENP.

As with the previous experiments [29–31], to understand the coherent amplification mechanism, it is helpful to compare actual data with results from numerical simulations. These simulations are based on the Maxwell–Bloch equations, which determine how the laser fields and the coherence develop within the ensemble.

The TPE process observed in our previous experiments is a four-wave mixing (FWM) process, which has been studied in nonlinear optics and quantum electronics [34]. In the current experiment setup, the frequencies of the two pump beams are identical, a process known as degenerate FWM (DFWM). Experiments to generate DFWM have been conducted using either the counter-propagating scheme [35, 36] or H<sub>2</sub> [37], although the motivations for those experiments differ substantially from the present motivation. Herein, we investigate TPE properties in detail through comparisons with simulation results.

The rest of this paper is structured as follows. In section 2, we note the properties of the p-H<sub>2</sub> molecule and describe the experimental setup. In section 3, we present the experimental results. In section 4, we compare these results with the results of numerical simulations. Details about the numerical simulations and the derivation of the Maxwell–Bloch equations are given in the appendix.

## 2. Experimental setup

Parahydrogen (p-H<sub>2</sub>) is a hydrogen molecule in which the spins of the two nuclei are antiparallel and thus the total nuclear spin angular momentum  $I_N$  is zero. The rotational

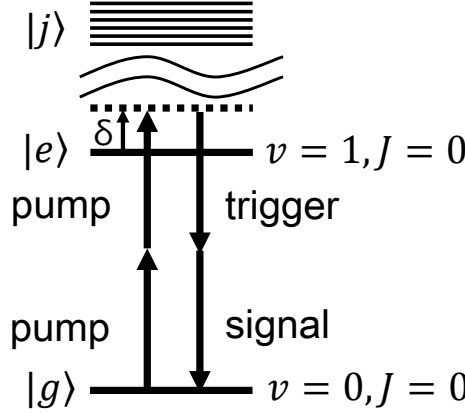


**Figure 1.** Schematic energy-level diagram of the parahydrogen molecule. The energy difference between the  $v = 0$  ground state  $|g\rangle$  and the  $v = 1$  vibrationally excited state  $|e\rangle$  corresponds to a wavelength of 2,403 nm. Intermediate states  $|j\rangle$  of the two-photon transitions are electronically excited states. The two-photon detuning  $\delta$  is defined as  $\delta = 2\omega_l - \omega_{eg}$ .

quantum numbers of p-H<sub>2</sub> in the electronic ground state are even ( $J = 0, 2, \dots$ ) because of the Pauli exclusion principle. At low temperatures, most p-H<sub>2</sub> molecules lie in the  $J = 0$  state.

To achieve huge rate amplification, it is favorable to use a target with small decoherence, and intermolecular interaction is a cause of decoherence. The intermolecular interactions of  $J = 0$  p-H<sub>2</sub> molecules are weaker than those of orthohydrogen molecules ( $I_N = 1$ , odd  $J$ ) because of the spherical symmetry of their rotational wavefunction. For this reason, we use a p-H<sub>2</sub> target rather than one involving normal hydrogen gas.

Figure 1 shows a schematic energy-level diagram of the p-H<sub>2</sub> molecule. We generate coherence between the ground state  $|g\rangle$  ( $v = 0, J = 0$ ) and the first vibrationally excited state  $|e\rangle$  ( $v = 1, J = 0$ ). The energy difference between  $|g\rangle$  and  $|e\rangle$  is  $\hbar\omega_{eg} = 0.5159$  eV. Single-photon electric dipole ( $E1$ ) transitions between these states are forbidden and two-photon  $E1 \times E1$  transitions are allowed. For this reason,  $|e\rangle$  is metastable and its spontaneous emission rate is  $\mathcal{O}(10^{-11})$  Hz, which is dominated by the two-photon  $E1 \times E1$  transition process [29]. The effect of the decoherence due to this spontaneous de-excitation is negligibly small in the present setup. The intermediate states  $|j\rangle$  of the two-photon transitions are electronically excited states. The energy-level differences between  $|g\rangle$  or  $|e\rangle$  and  $|j\rangle$ , namely  $\hbar\omega_{jg}$  and  $\hbar\omega_{je}$ , are much larger than  $\hbar\omega_{eg}$  (far-off-resonance condition). In the previous experiments to generate coherent TPE signals via one-sided excitation [29–31], we generated coherence between  $|g\rangle$  and  $|e\rangle$  using the Raman process, for which lasers with different frequencies were necessary. By contrast, in the present experiment we generate coherence using identical-frequency photons that originate from a single laser. This laser frequency is denoted by  $\omega_l$  and the two-photon detuning  $\delta$  is defined as  $\delta = 2\omega_l - \omega_{eg}$ .

The laser system is basically the same as that in the previous experiment in which third-harmonic generation was observed from the p-H<sub>2</sub> gas target [38]. We describe the laser system briefly here. Figure 2(a) shows the mid-infrared (MIR) laser system schematically. A continuous-wave (CW) laser ( $\lambda = 871.4$  nm) was prepared using an external-cavity diode laser (ECDL). The detuning  $\delta$  was controlled precisely by adjusting the frequency of the ECDL. The CW near-infrared (NIR) laser intensity was amplified by a tapered amplifier (TA). The CW laser was injected into a triangular cavity in which NIR laser pulses were generated in lithium triborate (LBO) crystals with the second harmonic of an injection-seeded Nd:YAG pulsed laser (Powerlite DLS 9010; Continuum;  $\lambda = 532.2$  nm) through optical parametric generation. Next, through optical parametric amplification in the LBO crystals, 1,367-nm pulses were generated from the pulsed NIR laser and the second harmonic of the injection-seeded Nd:YAG pulsed laser. The MIR pulses ( $\lambda = 4,806$  nm) were then generated through difference-frequency generation in potassium titanyl arsenate (KTA) crystals between the fundamental pulses of the injection-seeded Nd:YAG laser ( $\lambda = 1,064$  nm) and the 1,367-nm pulses. The repetition rate and duration of the MIR pulses were 10 Hz and roughly 5 ns (full width at half maximum (FWHM)), respectively. We measured the laser linewidth of the MIR pulses with absorption spectroscopy based on the rotational transitions of carbonyl sulfide gas. The estimated FWHM linewidth is  $145 \pm 16$  MHz, which is roughly 1.6 times larger than the Fourier-transform-limited linewidth if Gaussian-shaped pulses are assumed.

Figure 2(b) shows the experimental setup schematically. High-purity ( $> 99.9\%$ ) p-H<sub>2</sub> gas was prepared from normal hydrogen gas by using a magnetic catalyst (Fe(OH)O) cooled to approximately 14 K. The prepared p-H<sub>2</sub> gas was enclosed in a copper cell located inside a cryostat kept at approximately 78 K by liquid nitrogen. At this temperature, conversion from p-H<sub>2</sub> molecules to orthohydrogen molecules during the experiment was slow enough that the p-H<sub>2</sub> gas target needed to be replaced only once a week. The length of the cell was 15 cm, which was much shorter than the MIR pulse length. Anti-reflection-coated BaF<sub>2</sub> (WG01050-E; Thorlabs) substrates were used for the optical windows of the cryostat and the cell.

Beam splitters were used to divide the MIR beam into three beams. To excite the p-H<sub>2</sub> gas, counter-propagating pump MIR pulses (pump 1 and pump 2) were injected into the cell. The third beam, the trigger laser, was injected into the cell simultaneously with the pump beams to induce the TPE process. The timing jitter among the beams was negligibly small. The trigger beam was tilted by roughly 1° from the pump-beam axis in the horizontal direction so that the signal light was separated from the pump beams. The trigger beam almost overlapped with the pump beams around the center of the target cell. The diameters ( $D4\sigma$ ) of the input beams were 2–3 mm and were loosely focused around the center of the cell. The input pulse energies of the beams were measured by using an energy detector (QE12; Gentec-EO). The measured energies  $I_{p1}$  and  $I_{p2}$  of the pump beams were both roughly 1 mJ/pulse, and that of the trigger beam, namely,  $I_{trig}$ , was 0.6 mJ/pulse. The pulse-by-pulse fluctuation was roughly 10%.

The pump and trigger beams were circularly polarized using quarter-wave plates

before they were injected into the target. Both pump lasers were right-handed (RH) circularly polarized from the point of view of the source. The  $z$  axis is defined in figure 2(b). We chose the  $z$  axis as the quantization axis. The polarization of the pump-1 (pump-2) beam was  $\sigma^+$  ( $\sigma^-$ ) and the excitation by the pump-1 (pump-2) beam was a  $\Delta m_J = +1$  ( $\Delta m_J = -1$ ) process. Two-photon excitation with only the pump-1 beam or the pump-2 beam was forbidden because of the selection rule of the  $J = 0 \rightarrow J = 0$  two-photon transition. By contrast, two-photon excitation by the counter-propagating photon pair was allowed. The signal light was generated by the trigger pulse from the excited p-H<sub>2</sub> molecules and travelled back along the trigger beamline because of the amplification condition (momentum conservation). The trigger light was left-handed (LH) circularly polarized, and because of the selection rule the signal light was also LH circularly polarized. The p-H<sub>2</sub> molecules were allowed to be excited by the pump-1 laser and the trigger laser. However, in this case the direction of the de-excited photons was the same as that of the pump-1 or trigger laser because of the amplification condition, and these photons were not observed by the signal detector. Excitation by the pump-2 laser and the signal photons was also allowed, but its effect on the total signal intensity was negligibly small.

The signal light was horizontally polarized after it passed the quarter-wave plate. In this experiment, it was difficult to reduce the background component, which comprised scattered light from the pump and trigger beams. This is because the wavelength of that light was the same as that of the signal light, and therefore wavelength filters could not be used to reduce the stray background light. A portion of the signal light was reflected using a beam splitter (BSW511; Thorlabs) and was then reflected by a polarizing beam splitter (product 15625; Research Electro-Optics) that was used to reduce the background RH scattered light. Furthermore, the cryostat was placed on a rotation stage and was rotated to minimize the light of the pump and trigger beams reflected by the optical windows. The MIR signal pulses were detected using a mercury–cadmium–telluride detector (PC-3TE-9; Vigo System).

### 3. Results

#### 3.1. Detuning curve

First, we confirmed that the two-photon transition signal was generated from the p-H<sub>2</sub> target. The signal intensity was varied by changing the detuning  $\delta$  and could be separated from the background component. Figure 3 shows the observed spectra as functions of  $\delta$  for a target gas pressure of 280 kPa. For each detuning, we measured 200 or 300 signal pulses. The error bars in the plot indicate the standard errors, for which only the statistical uncertainty is considered. The signal intensity fluctuated because of the fluctuations of the positions and intensities of the input beams during the experiment. The systematic uncertainty, which includes these fluctuations, is much larger than the statistical uncertainty but is difficult to estimate and is not discussed

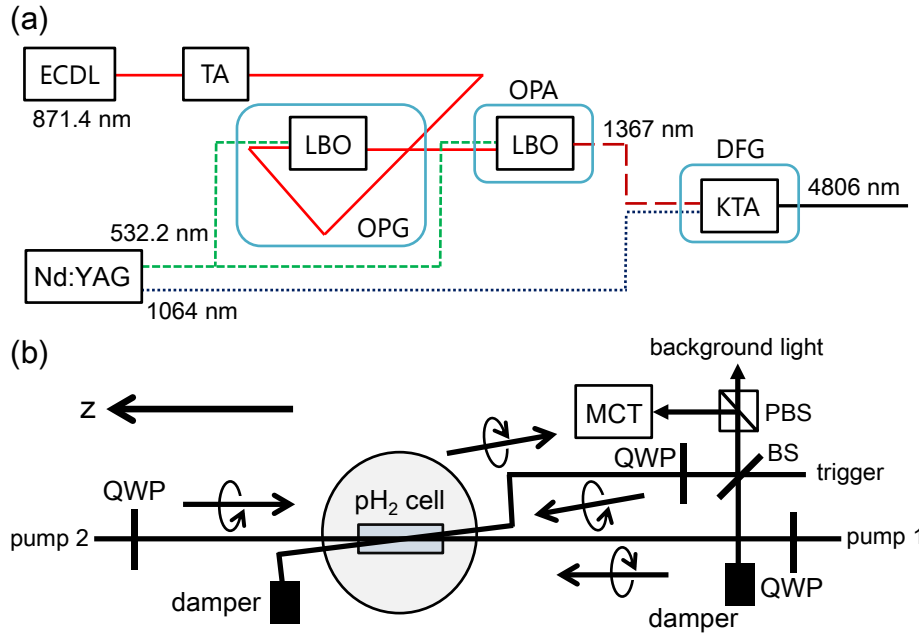


**Figure 2.** (a) Schematic of laser system with ECDL, TA, LBO crystals, and KTA crystals. (b) Schematic of experimental setup with quarter-wave plates (QWPs), beam splitter (BS), polarizing beam splitter (PBS), and mercury cadmium telluride (MCT) detector. The pump-1 (pump-2) beam was injected from the right (left) side of the figure. The trigger beam was injected from the right side of the figure.

further herein. For comparison, the distribution of signal intensity when the polarization of one of the pump lasers was changed to LH is shown as the blue squares. In this case, the two-photon excitation process was suppressed and only background scattered light was observed. This confirms that the signal peak stems from the TPE process.

The solid line in figure 3 is a fit to the data points of a Lorentzian function plus a constant, the latter representing the background component. As mentioned in section 2, the origin of  $\delta$  is defined as the point  $2\omega_l = \omega_{eg}$ . The MIR laser frequency was estimated during the experiment by monitoring the laser frequencies of the ECDL and the seed laser of the Nd:YAG laser with a high-precision wavemeter (WS-7; HighFinesse). Before conducting this experiment, we measured  $\omega_{eg}$  via the Raman scattering process between  $|g\rangle$  and  $|e\rangle$ . The previously measured  $\omega_{eg}$  was  $124,748.7 - 10.9 \times p$  GHz at 78 K, where  $p$  indicates the p-H<sub>2</sub> pressure in megapascals and the second term represents the pressure shift. This value is consistent with those measured in other experiments [39–41] within the systematic uncertainty of our measurement. The center value of the Lorentzian spectrum by the fit is  $-27$  MHz. The uncertainty of  $\delta$  is roughly 170 MHz, which was determined from the absolute accuracy of the wavemeter, and this center value is close to the origin.

By considering the detector responsivity and the transmittance of the optics, the signal energy  $I_{\text{sig}}$  around  $\delta = 0$  was estimated to be roughly 20 nJ. This value is of order

$10^{-5}$  times smaller than those of the pump and trigger pulses. The width of the fitted Lorentzian profile is described in section 3.3.

### 3.2. Dependence of signal energy on input pulse energies

Next, we show how the signal intensity depends on the intensities of the pump and trigger beams. To this end, we varied the input intensities of the MIR pulses by using neutral density (ND) filters. We placed these before the MIR pulses were divided into pump and trigger beams, and we varied the pump and trigger beam intensities at the same rate.

Figure 4 shows how the signal intensity depends on the input beam intensity at 288 kPa and  $\delta \approx 0$ . For each data point, we conducted approximately 3,000 measurements and subtracted the background component by using signal-intensity data measured at off-resonance points. The line is a fit to the experimental data of  $I_{\text{sig}} = A \times I^B$ , where  $I$  is the input pulse intensity before division and  $A$  and  $B$  are the fitting parameters. We obtained  $B = 2.99 \pm 0.03$ , although the actual systematic uncertainty is considered to be much larger than the obtained error.

### 3.3. Dependence of detuning curves on target pressure

Finally, we show how the detuning-curve width and signal intensity depend on the p-H<sub>2</sub> gas pressure. We varied the pressure of the target p-H<sub>2</sub> gas from 10 to 340 kPa. The signal intensities were weak, especially in the low-pressure region, and were largely affected by background light and detector noise. To confirm reproducibility, we measured several times in the 10–60 kPa region. We obtained the peak intensities and detuning-curve widths from the fitted curves of detuning dependence. We used the method of unweighted least squares to calculate the fitting errors.

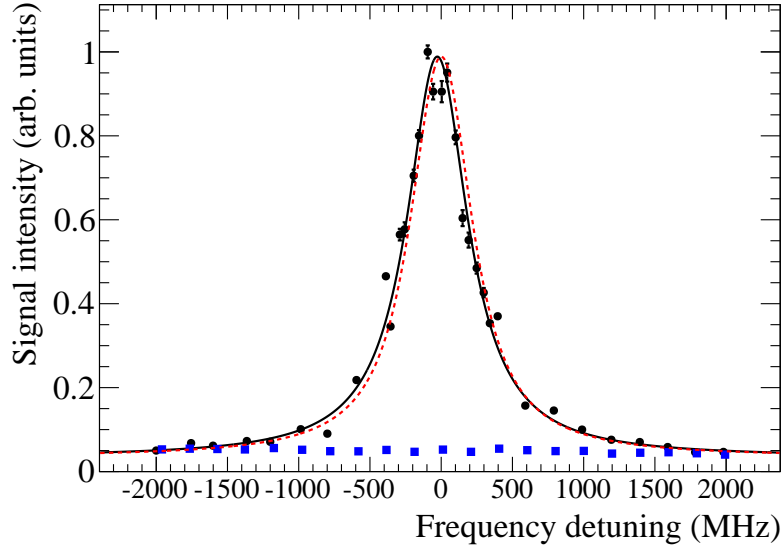
Figure 5 shows how the FWHM of the detuning curve depends on the target pressure. In the low-pressure region, the width of the detuning curve is considered to be dominated by the laser linewidth. The width of the detuning curve increases with the target pressure. This is due to the pressure broadening effect, the size of which is approximately proportional to the gas pressure [39].

Figure 6 shows how the peak signal intensity depends on the target pressure. The signal intensities are normalized by that at the highest pressure. The signal intensity increases with target density because more p-H<sub>2</sub> molecules are excited. However, the rate at which the signal intensity increases becomes lower because the decoherence effect due to pressure broadening is larger in the high-pressure region.

## 4. Discussion

### 4.1. Maxwell–Bloch equations

To understand the experimental results qualitatively, we constructed a numerical simulation that reproduces the experimental situation. The simulation is based on



**Figure 3.** Distributions of signal intensity as functions of detuning  $\delta$  for RH+RH polarized pump beams (black circles) and RH+LH polarized pump beams (blue squares). For each point, 200 or 300 signal pulses were measured. The error bars indicate standard errors. The black solid line is a fit to the black points of a Lorentzian function plus a constant, the latter representing the background component. The red dashed line is the normalized detuning curve of the simulation results with the same constant background.

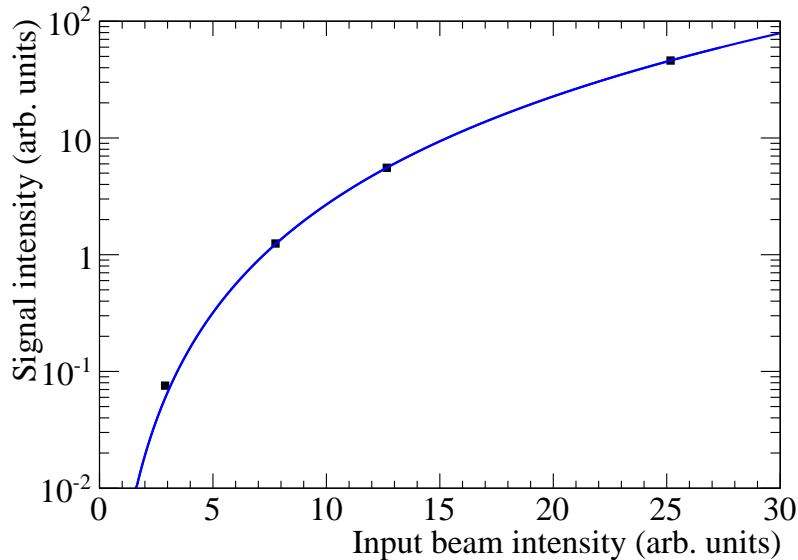


**Figure 4.** Dependence of signal intensity  $I_{\text{sig}}$  on input beam energy  $I$ . The black squares are experimental data. For each data point, approximately 3,000 measurements were made and the background component was subtracted by using data measured at off-resonance points. The blue solid line is a fit to the experimental data of  $I_{\text{sig}} = A \times I^B$ , where  $A$  and  $B$  are the fitting parameters.

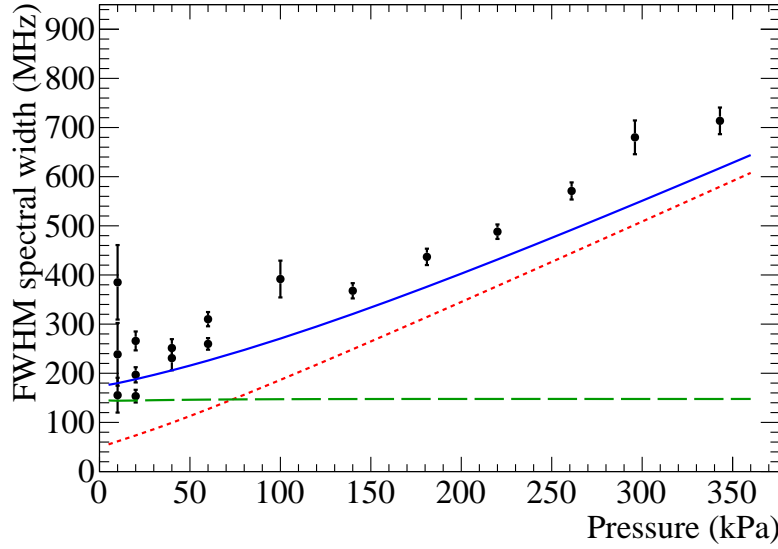


**Figure 5.** Dependence of spectral width of detuning curve on target pressure. The black circles are experimental data. In the low-pressure region, measurements were conducted several times to confirm reproducibility. The blue solid line shows the FWHM width of the simulation results. The red dotted line and green dashed line indicate the Lorentzian component and the Gaussian component of the Voigt width, respectively.

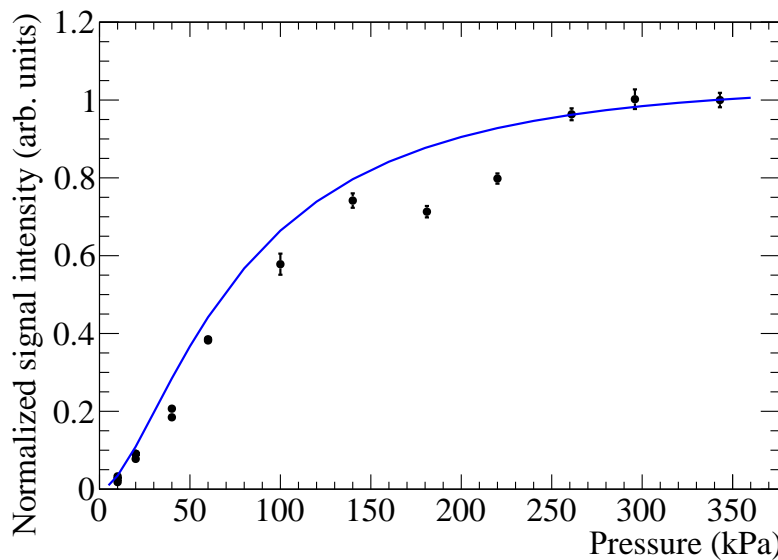


**Figure 6.** Dependence of peak signal intensity on target pressure. Signal intensities are normalized by that measured at the highest pressure. The black circles are experimental data. In the low-pressure region, measurements were conducted several times to confirm reproducibility. The blue line shows the simulation results.

the Maxwell–Bloch equations with one spatial and one temporal (1+1) dimension. In this simulation, we set the intensity and duration of the pump and trigger beams and the pressure of the p-H<sub>2</sub> gas target to the same values as those of the experiment. The temporal shapes of the input pulses are assumed to be Gaussian. We write the temporal electric-field distribution of each input beam at the target edge as

$$|E_X(t)|^2 = \frac{2c}{\varepsilon_0 \sqrt{2\pi} \sigma_t} I_X \exp\left(-\frac{(t - t_0 + L/2c)^2}{2\sigma_t^2}\right), \quad (4)$$

where  $I_X$  (X=p1, p2, trig),  $\sigma_t$ , and  $L$  indicate the pulse energy of each input beam, the duration of each pulse, and the target length, respectively. The centers of these beams pass through the target center at  $t = t_0$ . We describe here only the essential equations (we describe all the equations in the appendix), namely

$$\left(\frac{\partial}{\partial t} + c \frac{\partial}{\partial z}\right) E_{\text{sig}} \approx \frac{i\omega_l N_t}{2} (\alpha_{gg} E_{\text{sig}} + 2\alpha_{eg} \rho_{ge}^{0*} E_{\text{trig}}^*), \quad (5)$$

$$\frac{\partial \rho_{ge}^0}{\partial t} = -(i\delta + \gamma_2) \rho_{ge}^0 - i\Omega_{eg}^{0*}, \quad (6)$$

$$\Omega_{eg}^0 \approx \frac{\varepsilon_0 \alpha_{eg}}{2\hbar} E_{\text{p1}} E_{\text{p2}}. \quad (7)$$

Equation (5) represents the development of the envelope of the signal electric field  $E_{\text{sig}}$ ;  $N_t$  is the number density of the p-H<sub>2</sub> molecules, and  $\alpha_{gg}$  and  $\alpha_{eg}$  are the p-H<sub>2</sub> polarizabilities. Equation (6) represents the temporal development of the coherence generated by the pump lasers;  $\gamma_2$  is the transverse relaxation rate, and  $\Omega_{eg}^0$  is the two-photon Rabi frequency.

In the previous one-sided laser injection scheme, the Maxwellian part of the partial differential equations can be simplified to ordinary differential equations by introducing co-moving coordinates [29]. However, this treatment cannot be used for the counter-propagating injection scheme. Herein, we treat the partial differential equations directly by using the method of lines [42]. That treatment allows us to solve ordinary differential equations numerically with a discretized spatial derivative  $\partial/\partial z$ . To discretize the spatial derivative, we used weighted essentially non-oscillatory schemes [43].

In this simulation,  $\gamma_2$  is an input parameter. In previous one-sided-excitation experiments [13], we used the Raman transition linewidth  $\Delta_{\text{Raman}}$  between  $|g\rangle$  and  $|e\rangle$  as the value of  $2\gamma_2$ . The pressure dependence of  $\Delta_{\text{Raman}}$  is written approximately [39] as

$$\Delta_{\text{Raman}} = C_p p + \frac{C_D}{p}, \quad (8)$$

where  $p$  is the p-H<sub>2</sub> pressure and  $C_p$  and  $C_D$  are constants. The first term represents the pressure broadening effect and the second term represents the Doppler broadening effect with Dicke narrowing [44]. By contrast, the signal photons in the present experimental scheme were mostly generated from  $|e\rangle$  excited by the same-frequency counter-propagating pump lasers. Therefore, the system is almost Doppler-free [45, 46] and the residual Doppler effect is negligibly small compared with the other broadening effect. For this reason, we consider only the pressure broadening term for  $\gamma_2$ .

Equations (5)–(7) reveal that the signal intensity depends on the input signal energies and on  $\delta$ ,  $N_t$ , and  $\gamma_2$ . The detuning curves and how the signal energy depends on the input pulse energy and target pressure confirm that how the signal energy depends on these parameters is consistent between the measured data and the simulation results.

#### 4.2. Analytical estimation of signal-energy dependence on input pulse energies

We can predict how the signal energy depends on the input intensity by applying the Maxwell–Bloch equations to a simplified case in which we assume that the energies of the pump and trigger beams are constant. These signal energies actually decrease because of the two-photon absorption. From the simulation, the pump- and trigger-beam intensities are expected to decrease by around 1% after the beams pass through the target. Therefore, this treatment is a reasonable approximation. The temporal development of the coherence (equation (6)) is written as

$$\frac{\partial \rho_{ge}^0}{\partial t} = -(i\delta + \gamma_2)\rho_{ge}^0 - i\frac{c\alpha_{eg}}{\hbar\sigma_t\sqrt{2\pi}}\sqrt{I_{p1}I_{p2}}\exp\left(-\frac{(t-t_0)^2}{2\sigma_t^2} - \frac{z^2}{2\sigma_t^2c^2}\right), \quad (9)$$

where  $\sigma_t$  is the duration of each pulse. By considering the initial condition  $\rho_{ge}^0 = 0$  at  $t = -\infty$ , we obtain the solution of equation (9) as

$$\begin{aligned} \rho_{ge} = & -i\frac{c\alpha_{eg}}{2\hbar}\sqrt{I_{p1}I_{p2}}\exp\left(-\Gamma(t-t_0) + \frac{\sigma_t^2\Gamma^2}{2} - \frac{z^2}{2\sigma_t^2c^2}\right) \\ & \times \text{erfc}\left(\frac{-(t-t_0) + \sigma_t^2\Gamma}{\sqrt{2}\sigma_t}\right), \end{aligned} \quad (10)$$

where  $\Gamma = \gamma_2 + i\delta$  and “erfc” is the complementary error function. From equation (10),  $|\rho_{ge}^0|$  is proportional to  $\sqrt{I_{p1}I_{p2}}$ . In the governing equation for the signal electric field (equation (5)), the last term of the right-hand side represents the generation of signal photons induced by the trigger field. Because  $I_{\text{sig}} \propto |E_{\text{sig}}|^2$  is equivalent to

$$N_t^2|\rho_{ge}^0|^2I_{\text{trig}} \propto N_t^2I_{p1}I_{p2}I_{\text{trig}}, \quad (11)$$

the signal intensity  $I_{\text{sig}}$  has a cubic dependence on  $I$ . From the simulation, we also obtained  $I_{\text{sig}} = AI^x$ ,  $x \approx 3.0$ , where this approximation is not applied. The measured data are consistent with the theoretical predictions and the simulation results.

#### 4.3. Comparison of dependence of width of detuning curve on target pressure

The shape of the simulated detuning curve is approximated well by a Voigt profile, which is the convolution of a Lorentzian profile and a Gaussian profile. The red dashed line in figure 3 shows how the signal intensity depends on the detuning according to the simulations. Here, the signal intensity is normalized so that the peak height of the simulated detuning curve is the same as that of the fitted data. The shape of the simulated detuning curve is consistent with that of the fitted data.

The blue solid line in figure 5 shows the width of the simulated detuning curve. The experimental detuning curve is slightly wider than the simulated one. The width  $w_V$  of

the Voigt profile is approximated as  $w_V \approx 0.5346w_L + \sqrt{0.2166w_L^2 + w_G^2}$ , where  $w_L$  (red dotted line) and  $w_G$  (green dashed line) are the FWHMs of the Lorentzian and Gaussian functions, respectively [47]. In this case,  $w_L$  is almost linear with the p-H<sub>2</sub> pressure and  $w_G$  is almost constant. The Gaussian term arises from the Fourier-transform-limited laser linewidth. As mentioned in section 2, the actual laser linewidth is greater than the Fourier-transform-limited one. This is considered to be why the experimental and simulated detuning-curve widths differ.

The blue line in figure 6 shows how the simulated peak signal intensity depends on the pressure. The simulated signal intensity is normalized by that measured at the highest pressure. How the simulated normalized signal intensity depends on the pressure is again basically consistent with the experimental data. These results show that the decoherence of the system is dominated by the pressure broadening effect.

#### 4.4. Comparison of absolute signal energy

Finally, we compare the absolute signal energy between the simulations and the experiments. The simulated signal energy at 280 kPa and  $\delta = 0$  is roughly  $2.2 \times 10^2$  nJ, which is roughly 10 times larger than the experimental one.

The signal intensity depends largely on the relaxation rate. However, as described in section 4.3, how the simulated normalized signal intensity depends on the target pressure is consistent with the experiments, and it is unlikely that a wrongly estimated relaxation rate is causing the discrepancy. One possible reason for this discrepancy is that our numerical simulation is too simple. In particular, in this simulation we assume that the trigger and pump beams overlap completely throughout the target, which they did not in the actual experiment because the trigger beam was tilted from the pump beamline. By considering the beam overlap region inside the target, the signal intensity generated with this effect is estimated to be roughly half that when the beams overlap completely. However, the simulated peak signal intensity is still roughly five times larger than the experimental one. Another simplification is that we solved the 1+1-dimensional Maxwell–Bloch equations numerically without accounting for the transverse terms of the laser fields. This discrepancy might be resolved with more-realistic simulations, but that is beyond the scope of the present paper.

## 5. Conclusion

To deepen our understanding of the rate-amplification mechanism using atomic or molecular coherence, we conducted an experiment in which coherence was prepared by counter-propagating excitation laser pulses. We successfully observed the TPE signal from parahydrogen (p-H<sub>2</sub>) molecules. This observation is an important step for future neutrino spectroscopy experiments because the counter-propagating excitation scheme will be adopted in those experiments.

Another important advance is our improved understanding of the rate-amplification

mechanism through numerical simulations. We solved the Maxwell–Bloch equations numerically in one spatial and one temporal dimension. We compared the experimental signal energy and how it depended on the p-H<sub>2</sub> gas pressure and input beam energies with the equivalent calculated by numerical simulations, and we found qualitative consistency between the two.

## Acknowledgments

This work was supported by JSPS KAKENHI grant nos. JP15H02093, JP15H03660, JP15K13486, JP15K17651, JP16J10938, JP17K14292, JP17K14363, JP17K18779, JP17H02895, and JP17H02896. This work was also supported by JST PRESTO, and the Matsuo Foundation.

## Appendix A. Construction of simulation based on Maxwell–Bloch equations

In this appendix, we derive the Maxwell–Bloch equations and describe the numerical simulation.

### Appendix A.1. Laser field and parahydrogen states of experimental system

The electric fields of the pump, trigger, and signal lasers are represented as  $\tilde{\mathbf{E}}_{p1}$ ,  $\tilde{\mathbf{E}}_{p2}$ ,  $\tilde{\mathbf{E}}_{\text{trig}}$ , and  $\tilde{\mathbf{E}}_{\text{sig}}$ , respectively. We assume that the pump beams are RH circularly polarized and the trigger and signal beams are LH circularly polarized. To simplify the simulation and accelerate the numerical simulation, we conducted 1+1-dimensional simulations. We also ignored third-order and higher harmonics that are generated mainly through the two-photon excitation between the pump-1 and trigger beams. Our interest lies in the slowly varying envelopes of the electromagnetic fields. Because all the fields oscillate at a frequency close to the laser frequency  $\omega_l$  thanks to the simplification, they are expressed with the electromagnetic field envelopes ( $E_{p1}$ ,  $E_{p2}$ ,  $E_{\text{trig}}$ , and  $E_{\text{sig}}$ ) by

$$\tilde{\mathbf{E}}_{p1}(z, t) = \frac{1}{2} \left( E_{p1}(z, t) \hat{\epsilon}_R \exp\left(-i\omega_l(t - \frac{z}{c})\right) + (\text{c.c.}) \right), \quad (\text{A.1})$$

$$\tilde{\mathbf{E}}_{p2}(z, t) = \frac{1}{2} \left( E_{p2}(z, t) \hat{\epsilon}_R \exp\left(-i\omega_l(t + \frac{z}{c})\right) + (\text{c.c.}) \right), \quad (\text{A.2})$$

$$\tilde{\mathbf{E}}_{\text{trig}}(z, t) = \frac{1}{2} \left( E_{\text{trig}}(z, t) \hat{\epsilon}_L \exp\left(-i\omega_l(t - \frac{z}{c})\right) + (\text{c.c.}) \right), \quad (\text{A.3})$$

$$\tilde{\mathbf{E}}_{\text{sig}}(z, t) = \frac{1}{2} \left( E_{\text{sig}}(z, t) \hat{\epsilon}_L \exp\left(-i\omega_l(t + \frac{z}{c})\right) + (\text{c.c.}) \right), \quad (\text{A.4})$$

where  $\hat{\epsilon}_R$  and  $\hat{\epsilon}_L (= \hat{\epsilon}_R^*)$  represent circular-polarization unit vectors and  $\tilde{\mathbf{E}}$  or  $\tilde{E}$  indicate that electric fields include fast oscillating phase terms. Next, we denote the wavefunction of the p-H<sub>2</sub> system by

$$|\psi\rangle = c_g e^{-i\omega_g t} |g\rangle + c_e e^{-i(\omega_e + \delta)t} |e\rangle + c_{j+} e^{-i\omega_{j+} t} |j_+\rangle + c_{j-} e^{-i\omega_{j-} t} |j_-\rangle, \quad (\text{A.5})$$

where  $|j_+\rangle$  ( $|j_-\rangle$ ) represents the  $m_J = +1$  ( $m_J = -1$ ) intermediate states of p-H<sub>2</sub>. The Schrödinger equation of the system is

$$i\hbar \frac{\partial}{\partial t} |\psi\rangle = (H_0 + H_I) |\psi\rangle, \quad (\text{A.6})$$

where  $H_0$  is the free term of the p-H<sub>2</sub> states and  $H_I$  is the interaction Hamiltonian:

$$H_0 |g\rangle = \hbar\omega_g |g\rangle, \quad H_0 |e\rangle = \hbar\omega_e |e\rangle, \quad H_0 |j_{\pm}\rangle = \hbar\omega_j |j_{\pm}\rangle, \quad (\text{A.7})$$

$$H_I = -\mathbf{d} \cdot \tilde{\mathbf{E}} = -\mathbf{d} \cdot (\tilde{\mathbf{E}}_{\text{p1}} + \tilde{\mathbf{E}}_{\text{p2}} + \tilde{\mathbf{E}}_{\text{trig}} + \tilde{\mathbf{E}}_{\text{sig}}). \quad (\text{A.8})$$

$H_I$  comprises electric dipole interactions between  $|j_{\pm}\rangle$  and  $|g\rangle$  or  $|e\rangle$ . We also introduce the transition electric dipole moments  $d_{jg} = \langle j_{+(-)} | -\mathbf{d} \cdot \hat{\mathbf{e}}_{R(L)} | g \rangle$  and  $d_{je} = \langle j_{+(-)} | -\mathbf{d} \cdot \hat{\mathbf{e}}_{R(L)} | e \rangle$ . The other transition electric dipole moments are zero because they are  $E1$ -forbidden transitions.

### Appendix A.2. Optical Bloch equations

We derive the optical Bloch equations for the two-level reduced system and their approximation for the numerical simulation. First, we focus on  $|j_{\pm}\rangle$  of the Schrödinger equation (A.6):

$$\begin{aligned} i\hbar \frac{\partial c_{j+}}{\partial t} &= \frac{1}{2} (d_{jg} \exp(i\omega_{jg}t) c_g + d_{je} \exp(i\omega_{je}t) c_e) \left( \tilde{E}_{\text{p1}} + \tilde{E}_{\text{p2}}^* + \tilde{E}_{\text{trig}}^* + \tilde{E}_{\text{sig}} \right), \\ i\hbar \frac{\partial c_{j-}}{\partial t} &= \frac{1}{2} (d_{jg} \exp(i\omega_{jg}t) c_g + d_{je} \exp(i\omega_{je}t) c_e) \left( \tilde{E}_{\text{p1}}^* + \tilde{E}_{\text{p2}} + \tilde{E}_{\text{trig}} + \tilde{E}_{\text{sig}}^* \right), \end{aligned}$$

where we introduce  $\omega_{e'} = \omega_e + \delta$  and  $\omega_{je'} = \omega_j - \omega_e - \delta$ . By using the Markovian approximation and an initial condition ( $c_{j\pm}(t=0) = 0$ ), we obtain

$$\begin{aligned} c_{j+} &= -\frac{1}{2\hbar} \sum_m^{g,e'} d_{jm} c_m \left( \frac{\exp(i(\omega_{jm} - \omega_l)t) - 1}{\omega_{jm} - \omega_l} (\bar{E}_{\text{p1}} + \bar{E}_{\text{sig}}) \right. \\ &\quad \left. + \frac{\exp(i(\omega_{jm} + \omega_l)t) - 1}{\omega_{jm} + \omega_l} (\bar{E}_{\text{p2}}^* + \bar{E}_{\text{trig}}) \right), \end{aligned} \quad (\text{A.9})$$

$$\begin{aligned} c_{j-} &= -\frac{1}{2\hbar} \sum_m^{g,e'} d_{jm} c_m \left( \frac{\exp(i(\omega_{jm} - \omega_l)t) - 1}{\omega_{jm} - \omega_l} (\bar{E}_{\text{p2}} + \bar{E}_{\text{trig}}) \right. \\ &\quad \left. + \frac{\exp(i(\omega_{jm} + \omega_l)t) - 1}{\omega_{jm} + \omega_l} (\bar{E}_{\text{p1}}^* + \bar{E}_{\text{sig}}^*) \right), \end{aligned} \quad (\text{A.10})$$

where  $d_{je'} = d_{je}$  and  $c_{e'} = c_e$  and

$$\bar{E}_{\text{p1}} = E_{\text{p1}} \exp\left(i\omega_l \frac{z}{c}\right), \quad \bar{E}_{\text{p2}} = E_{\text{p2}} \exp\left(-i\omega_l \frac{z}{c}\right), \quad (\text{A.11})$$

$$\bar{E}_{\text{trig}} = E_{\text{trig}} \exp\left(i\omega_l \frac{z}{c}\right), \quad \bar{E}_{\text{sig}} = E_{\text{sig}} \exp\left(-i\omega_l \frac{z}{c}\right). \quad (\text{A.12})$$

By using equations (A.9) and (A.10) and the slowly varying envelope approximation, the original Schrödinger equation (A.6) is reduced to a Schrödinger equation of the two-level system,  $|g\rangle$  and  $|e\rangle$ :

$$i\hbar \frac{\partial c_g}{\partial t} = -\frac{\varepsilon_0 \alpha_{gg}}{4} c_g (|\bar{E}_{\text{p1}} + \bar{E}_{\text{sig}}|^2 + |\bar{E}_{\text{p2}} + \bar{E}_{\text{trig}}|^2)$$

$$- \frac{\varepsilon_0 \alpha_{eg}}{2} c_e (\bar{E}_{p1}^* + \bar{E}_{\text{sig}}^*) (\bar{E}_{p2}^* + \bar{E}_{\text{trig}}^*), \quad (\text{A.13})$$

$$\begin{aligned} i\hbar \frac{\partial c_e}{\partial t} = & -\hbar \delta c_e - \frac{\varepsilon_0 \alpha_{ee}}{4} c_g (|\bar{E}_{p1} + \bar{E}_{\text{sig}}|^2 + |\bar{E}_{p2} + \bar{E}_{\text{trig}}|^2) \\ & - \frac{\varepsilon_0 \alpha_{eg}^*}{2} c_e (\bar{E}_{p1} + \bar{E}_{\text{sig}}) (\bar{E}_{p2} + \bar{E}_{\text{trig}}), \end{aligned} \quad (\text{A.14})$$

where  $\alpha_{gg}$ ,  $\alpha_{ee}$ , and  $\alpha_{eg}$  represent the polarizabilities of hydrogen. They are given by

$$\alpha_{gg}(\omega) = \sum_j \frac{|d_{gj}|^2}{\varepsilon_0 \hbar} \left( \frac{1}{\omega_{jg} - \omega} + \frac{1}{\omega_{jg} + \omega} \right), \quad (\text{A.15})$$

$$\alpha_{ee}(\omega) = \sum_j \frac{|d_{je}|^2}{\varepsilon_0 \hbar} \left( \frac{1}{\omega_{je'} - \omega} + \frac{1}{\omega_{je'} + \omega} \right), \quad (\text{A.16})$$

$$\alpha_{eg}(\omega) = \sum_j \frac{d_{gj} d_{je}}{\varepsilon_0 \hbar} \frac{1}{\omega_{je'} + \omega}. \quad (\text{A.17})$$

We use an abbreviated notation  $\alpha_{gg,ee,eg}(\omega_l) = \alpha_{gg,ee,eg}$  for the case  $\omega = \omega_l$ . In this simulation, we accounted for most of the transitions via intermediate states, that is, the 0–36th vibrational transitions of the Lyman band and the 0–13th transitions of the Werner band [48].

The effective Hamiltonian of the two-level system is summarized by

$$i\hbar \frac{\partial}{\partial t} \begin{pmatrix} c_g \\ c_e \end{pmatrix} = H_{\text{eff}} \begin{pmatrix} c_g \\ c_e \end{pmatrix}, \quad H_{\text{eff}} = -\hbar \begin{pmatrix} \Omega_{gg} & \Omega_{ge} \\ \Omega_{eg} & \Omega_{ee} + \delta \end{pmatrix}, \quad (\text{A.18})$$

where  $\Omega_{ee}$  and  $\Omega_{gg}$  are the AC Stark shifts and  $\Omega_{eg}$  is the complex two-photon Rabi frequency.  $\Omega_{ee}$ ,  $\Omega_{gg}$ , and  $\Omega_{eg}$  are given by

$$\Omega_{gg} = \frac{\varepsilon_0 \alpha_{gg}}{4\hbar} (|\bar{E}_{p1} + \bar{E}_{\text{sig}}|^2 + |\bar{E}_{p2} + \bar{E}_{\text{trig}}|^2), \quad (\text{A.19})$$

$$\Omega_{ee} = \frac{\varepsilon_0 \alpha_{ee}}{4\hbar} (|\bar{E}_{p1} + \bar{E}_{\text{sig}}|^2 + |\bar{E}_{p2} + \bar{E}_{\text{trig}}|^2), \quad (\text{A.20})$$

$$\Omega_{eg} = \Omega_{ge}^* = \frac{\varepsilon_0 \alpha_{eg}}{2\hbar} (\bar{E}_{p1} + \bar{E}_{\text{sig}}) (\bar{E}_{p2} + \bar{E}_{\text{trig}}). \quad (\text{A.21})$$

To account for relaxation effects, we introduce the two-level density matrix by

$$\rho(z, t) = \begin{pmatrix} |c_g|^2 & c_g c_e^* \\ c_e c_g^* & |c_e|^2 \end{pmatrix} = \begin{pmatrix} \rho_{gg} & \rho_{ge} \\ \rho_{eg} & \rho_{ee} \end{pmatrix}, \quad (\text{A.22})$$

where  $|\rho_{ge}|$  is the coherence size. The time development of the density matrix (von Neumann equation or optical Bloch equations) including the relaxation effect is given by

$$\frac{\partial \rho_{gg}}{\partial t} = i(\Omega_{ge} \rho_{eg} - \Omega_{eg} \rho_{ge}) + \gamma_1 \rho_{ee}, \quad (\text{A.23})$$

$$\frac{\partial \rho_{ee}}{\partial t} = i(\Omega_{eg} \rho_{ge} - \Omega_{ge} \rho_{eg}) - \gamma_1 \rho_{ee} = -\frac{\partial \rho_{gg}}{\partial t}, \quad (\text{A.24})$$

$$\frac{\partial \rho_{ge}}{\partial t} = i(\Omega_{gg} - \Omega_{ee} - \delta) \rho_{ge} + i\Omega_{ge} (\rho_{ee} - \rho_{gg}) - \gamma_2 \rho_{ge}. \quad (\text{A.25})$$

Parameters  $\gamma_1$  and  $\gamma_2$  are the longitudinal and transverse relaxation rates, respectively, and represent the sizes of the decoherence effect. For the present setup, the longitudinal

relaxation comprises the natural lifetime of the excited state and the transit-time broadening, but  $\gamma_1$  is negligibly small compared with the laser duration. By contrast,  $\gamma_2$  has a large effect on the signal intensity.

In the Bloch equations,  $\Omega_{gg}$ ,  $\Omega_{ee}$ , and  $\Omega_{eg}$  include fast oscillating phases:

$$|\bar{E}_{p1} + \bar{E}_{\text{sig}}|^2 + |\bar{E}_{p2} + \bar{E}_{\text{trig}}|^2 = |E_{p1}|^2 + |E_{p2}|^2 + |E_{\text{trig}}|^2 + |E_{\text{sig}}|^2 + \left( E_{p1} E_{\text{sig}}^* \exp\left(2i\omega_l \frac{z}{c}\right) + E_{p2} E_{\text{trig}}^* \exp\left(-2i\omega_l \frac{z}{c}\right) + (\text{c.c.}) \right), \quad (\text{A.26})$$

$$(\bar{E}_{p1} + \bar{E}_{\text{sig}})(\bar{E}_{p2} + \bar{E}_{\text{trig}}) = E_{p1} E_{p2} + E_{\text{trig}} E_{\text{sig}} + E_{p1} E_{\text{trig}} \exp\left(2i\omega_l \frac{z}{c}\right) + E_{p2} E_{\text{sig}} \exp\left(-2i\omega_l \frac{z}{c}\right). \quad (\text{A.27})$$

Because it is difficult to treat such fast oscillating phase terms in our numerical simulations, we introduce further approximations. In this experimental setup, the AC Stark shift term in equation (A.25) is small ( $\max(|\Omega_{gg} - \Omega_{ee}|) = \mathcal{O}(1)$  MHz) compared with the laser linewidth and we ignore that term. Furthermore,  $\rho_{ee}$  is at most  $\mathcal{O}(10^{-5})$  and equation (A.25) is approximated to

$$\frac{\partial \rho_{ge}}{\partial t} = -(i\delta + \gamma_2) \rho_{ge} - i\Omega_{ge}. \quad (\text{A.28})$$

Finally, we separately consider fast oscillating terms in  $\rho_{ge}$  and  $\Omega_{eg}$  as

$$\rho_{ge} = \rho_{ge}^0 + \rho_{ge}^+ \exp\left(2i\omega_l \frac{z}{c}\right) + \rho_{ge}^- \exp\left(-2i\omega_l \frac{z}{c}\right), \quad (\text{A.29})$$

$$\Omega_{eg} = \Omega_{eg}^0 + \Omega_{eg}^+ \exp\left(2i\omega_l \frac{z}{c}\right) + \Omega_{eg}^- \exp\left(-2i\omega_l \frac{z}{c}\right), \quad (\text{A.30})$$

$$\Omega_{eg}^0 = \frac{\varepsilon_0 \alpha_{eg}}{2\hbar} (E_{p1} E_{p2} + E_{\text{trig}} E_{\text{sig}}), \quad (\text{A.31})$$

$$\Omega_{eg}^+ = \frac{\varepsilon_0 \alpha_{eg}}{2\hbar} E_{p1} E_{\text{trig}}, \quad \Omega_{eg}^- = \frac{\varepsilon_0 \alpha_{eg}}{2\hbar} E_{p2} E_{\text{sig}}, \quad (\text{A.32})$$

and each fast frequency component of equation (A.28) becomes

$$\frac{\partial \rho_{ge}^0}{\partial t} = -(i\delta + \gamma_2) \rho_{ge}^0 - i\Omega_{eg}^{0*}, \quad (\text{A.33})$$

$$\frac{\partial \rho_{ge}^+}{\partial t} = -(i\delta + \gamma'_2) \rho_{ge}^+ - i\Omega_{eg}^{-*}, \quad (\text{A.34})$$

$$\frac{\partial \rho_{ge}^-}{\partial t} = -(i\delta + \gamma'_2) \rho_{ge}^- - i\Omega_{eg}^{+*}. \quad (\text{A.35})$$

The coherence components (i)  $\rho_{ge}^0$ , (ii)  $\rho_{ge}^+$ , and (iii)  $\rho_{ge}^-$  represent the coherence generated by the fields of (i) pump 1 + pump 2 and trigger + signal, (ii) pump 2 + signal, and (iii) pump 1 + trigger, respectively. The population development (equations (A.23) and (A.24)) still includes fast oscillating terms, but as shown in section A.3 the signal intensity does not depend on the population by adopting the approximation  $\rho_{ee} \ll \rho_{gg} \simeq 1$ .

In the simulations used in our previous experiments [31], we calculated  $\gamma_2$  from the Raman linewidths (equation (8)) of an external experiment [39] as an approximation. In the present simulation, we used the same value for  $\gamma'_2$  in equations (A.34) and (A.35). However, as described in section 4.1, the Doppler broadening effect is negligible for

excitation by counter-propagating lasers. Therefore, the value of  $\gamma_2$  in equation (A.33) is calculated from only the pressure broadening term of the Raman linewidth.

### Appendix A.3. Maxwell equations

We also consider how the laser fields develop and the macroscopic polarization of the p-H<sub>2</sub> molecules. Maxwell's equations in a homogeneous dielectric gas medium without sources and magnetization are given by

$$\begin{aligned}\nabla \cdot \tilde{\mathbf{D}} &= 0, & \nabla \cdot \tilde{\mathbf{B}} &= 0, \\ \nabla \times \tilde{\mathbf{E}} &= -\frac{\partial}{\partial t} \tilde{\mathbf{B}}, & \nabla \times \tilde{\mathbf{B}} &= \mu_0 \frac{\partial}{\partial t} \tilde{\mathbf{D}}, \\ \tilde{\mathbf{D}} &= \varepsilon_0 \tilde{\mathbf{E}} + N_t \tilde{\mathbf{P}}, & \nabla \cdot \tilde{\mathbf{E}} &= 0,\end{aligned}$$

where  $N_t$  is the number density of the p-H<sub>2</sub> molecules, and  $\tilde{\mathbf{E}}$  and  $\tilde{\mathbf{P}}$  are the laser fields and the macroscopic polarization of the p-H<sub>2</sub> molecules, respectively. From these equations, developments of the laser fields propagating in the  $z$  direction are given by

$$\frac{\partial^2 \tilde{\mathbf{E}}}{\partial t^2} - c^2 \frac{\partial^2 \tilde{\mathbf{E}}}{\partial z^2} = -\frac{N_t}{\varepsilon_0} \frac{\partial^2 \tilde{\mathbf{P}}}{\partial t^2}. \quad (\text{A.36})$$

In the present experimental setup,  $\tilde{\mathbf{E}}$  and  $\tilde{\mathbf{P}}$  are written as

$$\tilde{\mathbf{E}} = \tilde{\mathbf{E}}_{\text{p1}} + \tilde{\mathbf{E}}_{\text{p2}} + \tilde{\mathbf{E}}_{\text{trig}} + \tilde{\mathbf{E}}_{\text{sig}}, \quad (\text{A.37})$$

$$-\tilde{\mathbf{P}} = -\langle \psi | \mathbf{d} | \psi \rangle \quad (\text{A.38})$$

$$= (c_{j-}^* c_g e^{i\omega_{jg} t} d_{jg} + c_g^* c_{j+} e^{i\omega_{gj} t} d_{gj} + c_e^* c_{j+} e^{i\omega_{ej} t} d_{ej} + c_{j-}^* c_e e^{i\omega_{je} t} d_{je}) \hat{\epsilon}_R + (\text{c.c.}).$$

By using equations (A.9) and (A.10) and ignoring all the frequency components other than  $\exp(\pm i\omega_l t)$ , equation (A.38) becomes

$$\begin{aligned}\frac{2}{\varepsilon_0} \tilde{\mathbf{P}} &= \left[ ((\alpha_{gg} \rho_{gg} + \alpha_{ee} \rho_{ee}) E_{\text{p1}} + 2\alpha_{eg} \rho_{ge}^* E_{\text{p2}}^*) \exp\left(-i\omega_l \left(t - \frac{z}{c}\right)\right) \right. \\ &\quad + ((\alpha_{gg} \rho_{gg} + \alpha_{ee} \rho_{ee}) E_{\text{sig}} + 2\alpha_{eg} \rho_{ge}^* E_{\text{trig}}^*) \exp\left(-i\omega_l \left(t + \frac{z}{c}\right)\right) \\ &\quad + ((\alpha_{gg} \rho_{gg} + \alpha_{ee} \rho_{ee}) E_{\text{p2}}^* + 2\alpha_{eg}^* \rho_{ge} E_{\text{p1}}) \exp\left(i\omega_l \left(t + \frac{z}{c}\right)\right) \\ &\quad \left. + ((\alpha_{gg} \rho_{gg} + \alpha_{ee} \rho_{ee}) E_{\text{trig}}^* + 2\alpha_{eg}^* \rho_{ge} E_{\text{sig}}) \exp\left(i\omega_l \left(t - \frac{z}{c}\right)\right) \right] \hat{\epsilon}_R \\ &\quad + (\text{c.c.}).\end{aligned} \quad (\text{A.39})$$

By using the approximations

$$\alpha_{gg} \rho_{gg} + \alpha_{ee} \rho_{ee} \simeq \alpha_{gg}, \quad (\text{A.40})$$

$$\left( \frac{\partial}{\partial t} \pm i\omega_l \right) (\text{slowly varying term}) \simeq \pm i\omega_l (\text{slowly varying term}), \quad (\text{A.41})$$

$$\left( c \frac{\partial}{\partial z} \pm i\omega_l \right) (\text{slowly varying term}) \simeq \pm i\omega_l (\text{slowly varying term}), \quad (\text{A.42})$$

we obtain the developments of the envelopes of the electric fields:

$$\left( \frac{\partial}{\partial t} - c \frac{\partial}{\partial z} \right) E_{\text{p1}} = \frac{i\omega_l N_t}{2} (\alpha_{gg} E_{\text{p1}} + 2\alpha_{eg} (\rho_{ge}^{0*} E_{\text{p2}}^* + \rho_{ge}^{-*} E_{\text{trig}}^*)), \quad (\text{A.43})$$

$$\left( \frac{\partial}{\partial t} + c \frac{\partial}{\partial z} \right) E_{\text{p2}} = \frac{i\omega_l N_t}{2} (\alpha_{gg} E_{\text{p2}} + 2\alpha_{eg} (\rho_{ge}^{0*} E_{\text{p1}}^* + \rho_{ge}^{+*} E_{\text{sig}}^*)) , \quad (\text{A.44})$$

$$\left( \frac{\partial}{\partial t} - c \frac{\partial}{\partial z} \right) E_{\text{trig}} = \frac{i\omega_l N_t}{2} (\alpha_{gg} E_{\text{trig}} + 2\alpha_{eg} (\rho_{ge}^{0*} E_{\text{sig}}^* + \rho_{ge}^{-*} E_{\text{p1}}^*)) , \quad (\text{A.45})$$

$$\left( \frac{\partial}{\partial t} + c \frac{\partial}{\partial z} \right) E_{\text{sig}} = \frac{i\omega_l N_t}{2} (\alpha_{gg} E_{\text{sig}} + 2\alpha_{eg} (\rho_{ge}^{0*} E_{\text{trig}}^* + \rho_{ge}^{+*} E_{\text{p2}}^*)) . \quad (\text{A.46})$$

As evident from these equations, signal photons are generated by the trigger field with  $\rho_{ge}^0$  and the pump-2 field with  $\rho_{ge}^+$ . Because  $\rho_{ge}^+$  is developed by the pump-2 + signal fields and  $|\rho_{ge}^+|$  is small, most of the signal light is generated by the trigger field, with the coherence generated by the pump beams.

## References

- [1] Dicke R H 1954 *Phys. Rev.* **93** 99
- [2] Skribanowitz N, Herman I P, MacGillivray J C and Feld M S 1973 *Phys. Rev. Lett.* **30** 309
- [3] Gross M, Fabre C, Pillet P, and Haroche S 1976 *Phys. Rev. Lett.* **36** 1035
- [4] Kaluzny Y *et al* 1983 *Phys. Rev. Lett.* **51** 1175
- [5] DeVoe R G and Brewer R G 1996 *Phys. Rev. Lett.* **76** 2049
- [6] Yoshikawa Y, Sugiura T, Torii Y and Kuga T 2004 *Phys. Rev. A* **69** 041603
- [7] Brandes T 2005 *Phys. Rep.* **408** 315
- [8] Scheibner M *et al* 2007 *Nat. Phys.* **3** 106
- [9] Scully M O 2015 *Phys. Rev. Lett.* **115** 243602
- [10] Gross M and Haroche S 1982 *Phys. Rep.* **93** 301
- [11] Cui N and Macovei M A 2017 *Phys. Rev. A* **96** 063814
- [12] Yoshimura M *et al* 2008 arXiv:0805.1970
- [13] Fukumi A *et al* 2012 *Prog. Theor. Exp. Phys.* **2012** 04D002
- [14] Yoshimura M 2007 *Phys. Rev. D* **75** 113007
- [15] Abe K *et al* (Super-Kamiokande Collaboration) 2016 *Phys. Rev. D* **94** 052010
- [16] Gando A *et al* (KamLAND Collaboration) 2013 *Phys. Rev. D* **88** 033001
- [17] F P An *et al* (Daya Bay Collaboration) 2017 *Phys. Rev. D* **95** 072006
- [18] Abe K *et al* (T2K Collaboration) 2017 *Phys. Rev. D* **96** 092006
- [19] Adamson P *et al* (NOvA Collaboration) 2017 *Phys. Rev. Lett.* **118** 231801
- [20] Giganti C, Lavignac S and Zito M 2018 *Prog. Part. Nucl. Phys.* **98** 1
- [21] Drexlin G, Hannen V, Mertens S and Weinheimer C 2013 *Adv. High Energy Phys.* **2013** 293986
- [22] Ade P A R *et al* (Planck Collaboration) 2016 *Astron. Astrophys.* **594** A13
- [23] Esteban I *et al* 2017 *J. High Energ. Phys.* **2017** 87
- [24] Päs H and Rodejohann W 2015 *New J. Phys.* **17** 115010
- [25] Lesgourgues J and Pastor S 2014 *New J. Phys.* **16** 065002
- [26] Dinh D N *et al* 2012 *Phys. Lett. B* **719** 154
- [27] Tanaka M *et al* 2017 *Phys. Rev. D* **96** 113005
- [28] Song N *et al* 2016 *Phys. Rev. D* **93** 013020
- [29] Miyamoto Y *et al* 2014 *Prog. Theor. Exp. Phys.* **2014** 113C01
- [30] Miyamoto Y *et al* 2015 *Prog. Theor. Exp. Phys.* **2015** 081C01
- [31] Hara H *et al* 2017 *Phys. Rev. A* **96** 063827
- [32] Yoshimura M and Sasao N 2014 *Prog. Theor. Exp. Phys.* **2014** 073B02
- [33] Yoshimura M, Sasao N and Tanaka M 2012 *Phys. Rev. A* **86** 013812
- [34] He G S 2002 *Prog. Quant. Electron.* **26** 131
- [35] Kauranen M, Gauthier D J, Malcuit M S and Boyd R W 1988 *Opt. Lett.* **13** 663
- [36] Kauranen M and Boyd R W 1991 *Phys. Rev. A* **44** 584

- [37] Meijer G and Chandler D W 1992 *Chem. Phys. Lett.* **192** 1
- [38] Miyamoto Y *et al* 2018 *J. Phys. B* **51** 015401
- [39] Bischel W K and Dyer M J 1986 *Phys. Rev. A* **33** 3313
- [40] Dickenson G D *et al* 2003 *Phys. Rev. Lett.* **110**, 193601
- [41] Rahn L A and Rosasco G J 1990 *Phys. Rev. A* **41** 3698
- [42] Hamdi S, Schiesser W E and Griffiths G W 2007 Scholarpedia **2** 2859
- [43] S C Wang 2009 *SIAM Rev.* **51** 82
- [44] Dicke R H 1953 *Phys. Rev.* **89** 472
- [45] Firstenberg O *et al* 2007 *et al* *Phys. Rev. A* **76** 013818
- [46] Shuker M *et al* 2007 *Phys. Rev. A* **76** 023813
- [47] Olivero J J and Longbothum R L 1977 *J. Quant. Spectrosc. Radiat. Transfer* **17** 233
- [48] Huang S W, Chen W J and Kung A H 2006 *Phys. Rev. A* **74** 063825